Available online at www.sciencedirect.com

jmr&t Journal of Materials Research and Technology

journal homepage: www.elsevier.com/locate/jmrt

Short Communication

High CO_2 reduction activity on AlCrCoCuFeNi multi-principal element alloy nanoparticle electrocatalysts prepared by means of pulsed laser ablation

H. Pérez Blanes [a,b], *P. Ghiasi* [a,c], *J. Sandkühler* [a,d], *Y. Yesilcicek* [a], *S. Pentzien* [a], *A. Conradi* [a], *C. Prinz* [a], *D. Al-Sabbagh* [a], *A.F. Thünemann* [a], *O. Ozcan* [a], *J. Witt* [a,*]

[a] *Bundesanstalt für Materialforschung und -prüfung (BAM), Berlin, Germany*
[b] *Universitat Ramon Llull IQS, Barcelona, Spain*
[c] *Technische Universität Berlin, Berlin, Germany*
[d] *Hochschule Merseburg, Merseburg, Germany*

ARTICLE INFO

Article history:
Received 10 March 2023
Accepted 15 May 2023
Available online 19 May 2023

Keywords:
Multi-principal element alloys
Electrocatalysis
Carbon dioxide reduction
Nanoparticles
Pulsed laser ablation
Transmission electron microscopy

ABSTRACT

Noble metal-free nanoparticles (NPs) based on multi-principal element alloys (MPEAs) were synthesized using a one-step pulsed laser ablation in liquids (PLALs) method for the electrochemical reduction of CO_2. Laser ablation was performed in pure water or poly-(diallyldimethylammonium chloride) (PDADMAC)-containing an aqueous solution of $Al_8Cr_{17}Co_{17}Cu_8Fe_{17}Ni_{33}$ MPEA targets. Transmission electron microscopy (TEM) measurements combined with energy dispersive X-ray (EDX) mapping were used to characterize the structure and composition of the laser-generated MPEA nanoparticles (MPEA-NPs). These results confirmed the presence of a characteristic elemental distribution of a core-shell phase structure as the predominant NP species. The electrocatalytic performance of the laser-generated MPEA-NPs was characterized by linear sweep voltammetry (LSV) demonstrating an enhanced electrocatalytic CO_2 activity for PDADMAC-stabilized NPs. The findings of these investigations indicate that MPEAs have great potential to replace conventional, expensive noble metal electrocatalysts.

1. Introduction

The use of nano-sized multi-principal element alloys (MPEAs) as electrocatalysts has the potential to provide a more cost-effective and efficient alternative to noble metal electrocatalysts [1,2]. The multi-elemental mixture and the high configurational entropy of MPEAs offer advantages in tailored catalytic activity, product selectivity, and improved stability under harsh conditions.

* Corresponding author.
E-mail address: julia.witt@bam.de (J. Witt).
https://doi.org/10.1016/j.jmrt.2023.05.143

The equiatomic CrMnFeCoNi alloy is the most widely studied MPEA due to its versatile properties. It has been shown to have a comparable catalytic activity for the hydrogen evolution reaction (HER) to that of Pt [3]. In addition, CoMoFeNiCu-nanoparticles (NPs) have been shown to efficiently decompose ammonia to hydrogen [4]. Due to the high surface area to volume ratio and the complexity of mixing, the MPEA-NPs provide multiple active sites for reactions that require different catalysts for each step. In their pioneering work, Nellaiappan et al. [5] demonstrated the use of AuAgPdPtCu-NPs for the electrocatalytic CO_2 reduction reaction (CO_2RR). The active sites were predominantly redox-active Cu-species (Cu^{2+}/Cu^0), whereas other metals provided a synergistic effect. This catalytic system exhibited a high CO_2 activity achieving a faradaic efficiency of about 100% towards gaseous products even at low potential (−0.3 V vs. RHE) compared to catalysts based on pure Cu.

The size and chemical composition of NPs is critical for their catalytic applications. Pulsed laser ablation in liquids (PLALs) provides an environmentally friendly and cost-effective method for synthesizing NPs directly from bulk materials compared to chemical routes [6,7]. Furthermore, the implementation of remote-controlled approaches represents a significant advancement in enhancing the safety and efficiency standards for off-site real-time monitoring of experimental equipment in many scientific and industrial laboratories [8]. This method is gaining popularity for the synthesis of multi-element NPs that are difficult to produce using wet chemical synthesis methods due to its rapid NP formation kinetics [9–11]. PLAL has been used to synthesize various bimetallic particles, including Cu-Zn [12], Ag–Cu [13], Fe–Rh [14], Ni–Pd, and Au–Ag [15]. Recently, for the first time, the synthesis of NPs from CrCoFeNiMn with an equimolar stoichiometry and a diameter of less than 5 nm was reported [16].

Cu-based electrocatalysts are the most promising catalyst system because Cu is so far the only metal capable of converting CO_2 into multiple-carbon products under mild reaction conditions, and at the same time it offers a cost-effective alternative to noble metal catalysts [17–19]. However, monometallic Cu-electrocatalysts are still limited by their poor product selectivity and high overpotential for the CO_2RR application. Many published research results demonstrated that bimetallic systems combining Cu with another metal have shown enhanced catalytic properties for the electrochemical reduction of CO_2 [20–24]. The alloy-dependent property can be attributed to the electronic structure, which can be tuned depending on the atomic ratio, or the element combinations of the Cu-based alloys used, thus affecting the catalytic activity or adsorption of intermediates and reactants [25–27]. In the literature, the design of Cu-containing noble metal-free MPEAs as catalysts for the CO_2RR has only been reported using a computational approach, such as combined density functional theory (DFT) and supervised machine learning to predict the CO and hydrogen adsorption energies of all surface sites on (111) surfaces of the disordered CoCu-GaNiZn and AgAuCuPdPt MPEAs [28].

In this study, a noble metal-free Cu-based MPEA has been developed for CO_2RR. Colloidal MPEA-NPs were synthesized with and without polymer stabilization by PLAL. Transmission electron microscopy (TEM) combined with energy dispersive X-ray (EDX) mapping was used to characterize the structure and composition of the laser-generated MPEA-NPs. Electrochemical analysis showed enhanced electrocatalytic activity of PDADMAC-stabilized MPEA-NPs for the CO_2RR.

2. Experimental

2.1. Sample preparation

The as-cast $Al_8Cr_{17}Co_{17}Cu_8Fe_{17}Ni_{33}$ MPEA was prepared with the AM200 vacuum arc melter (Edmund Bühler GmbH, Germany) using 99.99% purity metals (Goodfellow, Germany). To eliminate dendritic segregation and produce a single-phase structure, the alloy was heat-treated at 1250 °C for 1 h under Ar atmosphere followed by quenching in ice water. Prior to use, specimen surfaces were mechanically wet ground using SiC-papers (ATM GmbH, Germany) up to a grit size of 4000 and then polished with 3 and 1 μm diamond monocrystalline paste (ATM GmbH, Germany). For final polishing colloidal silicon dioxide nanoparticles with a diameter of 50 nm were used (ATM GmbH, Germany). Finally, the samples were cleaned in an ultrasonic bath for 5 min in ethanol (98%, Sigma Aldrich, Germany) and dried in an air stream.

PLAL synthesis of MPEA-NPs was performed with a *TruMicro 5050 Femto Edition* (Trumpf, Germany) laser setup. The setup used 925-fs pulses with a maximum pulse energy of 100 μJ, a repetition rate of 400 kHz at a wavelength of 1030 nm under mild stirring. A laser scanning geometry with a scan speed of 50 mm s^{-1} at a repetition rate of 100 kHz was used. The laser energy density was ~24 J cm^{-2}. NPs generated in water and in poly(diallyldimethylammonium chloride) (PDADMAC)-containing (0.2-wt%) aqueous solution were referred as non-stabilized (NS-NPs) and polymer-stabilized nanoparticles (PS-NPs), respectively. 25 mL of the NP suspension was centrifuged at 27,000 g for 15 min and 30,000 g for 20 min at 15 °C (5424 R Eppendorf®centrifuge). The supernatant solution was removed, and the NP-pellet was redispersed in 5 mL of deionized water using an ultrasonic probe (HD 3200, Bandelin, Germany) for 5 min. The MPEA-NPs were then loaded onto a glassy carbon (GC) rotating disk electrode (RDE) with a surface area of 0.126 cm^2 according to a literature procedure [19]. The method involved initial preparation of a stock solution with 0.2 mL isopropanol (Sigma Aldrich), 0.004 mL of 5 wt% Nafion ionomer solution (Sigma-Aldrich) and 1 mL of NP suspension. The stock solution was sonicated for 30 min. The dispersion (10 μL) was deposited on a clean GC electrode and spun at 900 rpm until the liquid was evaporated. Prior to use GC electrodes were polished with 0.3 mm and 0.05 mm alumina powder and sonicated with deionized water for 5 min to remove contaminations.

2.2. Sample characterization

Electrochemical analysis was conducted on the MPEA-ingots and NP-electrodes using a three-electrode setup and a RDE with a Gamry Reference 600+ potentiostat (Gamry

Instruments, USA). The measurements were performed in 0.5 M K_2CO_3 (pH 11.8) after degassing with N_2 and CO_2 for 30 min, using a Pt counter electrode and an Ag/AgCl (3 M NaCl, ALS Co., Japan) reference electrode. The potential conversion to reversible hydrogen electrode (RHE) was calculated using the following equation:

$$E_{RHE} = E_{Ag/AgCl} + (0.209 + 0.059\ pH) \quad (1)$$

Linear sweep voltammetry (LSV) and cyclic voltammetry (CV) experiments were performed in a potential range of 0 to −1.6 V (vs. Ag/AgCl) at a scan rate of 20 and 50 mV s^{-1}, respectively. The macroscopic surface area of the sample was 0.636 cm^2.

The structure and chemical composition of MPEAs were investigated by scanning electron microscopy (SEM) and energy dispersive X-ray spectroscopy (EDX), with a Tescan Vega 3 XLH equipped with X Max 80 detector (Oxford Instruments). X-Ray diffraction (XRD) data were collected using a Bruker D8 Advance diffractometer (Bruker AXS, Germany) in Bragg-Brentano Geometry with a Lynxeye-detector using Cu-Kα radiation ($\lambda = 1.542$ Å) over a range of $2\theta = 10°–130°$ with a step size of 0.02°.

Transmission electron microscopy (TEM) images of MPEA-NPs were acquired using a Talos F200S Microscope (Thermo Fisher Scientific, Netherlands) operated at 200 kV. A Ceta 16 M camera, a high-angle annular dark-field (HAADF) and bright field (BF) detector (STEM mode; Scanning transmission electron microscopy) were used to capture the images. The specimens were prepared by dropping sample solutions (~10 μL NP-suspension) onto a 3 mm gold grid (Plano, 300 mesh) and drying at room temperature (RT). Elemental analysis of the NPs was performed using EDX, with two silicon drift detectors (SDD) and a counting time of 60 s.

Small angle X-ray scattering (SAXS) measurements were performed in a flow through capillary using a Kratky-type instrument (SAXSess from Anton Paar, Austria) with a low sample-to-detector distance of 0.309 m at a temperature of (21 ± 1) °C. The measured intensity was converted to absolute scale according to Orthaber et al. [29], and the scattering vector was defined as $q = 4\pi n/\lambda \sin\theta$, where q is the scattering angle and λ the wavelength of the radiation ($\lambda = 0.154$ nm). Deconvolution of the SAXS curves was performed with the SAXS-Quant software. Curve fitting was conducted with SASfit software [30].

3. Results and discussion

3.1. Microstructural characterization of the $Al_8Cr_{17}Co_{17}Cu_8Fe_{17}Ni_{33}$ MPEA

As the microstructure of the $Al_8Cr_{17}Co_{17}Cu_8Fe_{17}Ni_{33}$ MPEA is very sensitive to the Al level [31] and the phase diagram of the Cu–Fe, Cu–Cr and Cu–Co systems include a broad miscibility gap [32,33], the combination of all elements in one alloy without phase separation and segregation is not straightforward. The SEM images of the (a) as-cast and (b) homogenized $Al_8Cr_{17}Co_{17}Cu_8Fe_{17}Ni_{33}$ are presented in Fig. 1.

The SEM image in Fig. 1a displays a representative microstructure of the as-cast samples, where severe element segregations are visible as bright dendritic regions located at the grain boundaries. The matrix is imaged with light and dark gray areas. This observation can be attributed to the orientation contrast effect, since the BSE signal intensity varies with the crystallographic orientation of domains within the sample. The homogenized samples show micropores and large grains in the range of 50–350 μm (Fig. 1b) with different crystallographic orientations, indicated by varying gray levels of the grains. The corresponding XRD spectrum in Fig. 1c indicates the presence of a face-centered cubic (fcc) crystal system after the homogenization process. Due to the large grain size, not all orientations are detected, but the results are consistent with those reported in the literature [34]. EDX maps of the as-cast sample confirmed that the dendrites were enriched in Al, Cu and Ni and depleted in Co, Cr and Fe (Fig. 2a). After homogenization, the dendritic structure was completely dissolved, resulting in a homogeneous distribution of elements (Fig. 2b). The homogenized MPEA is used in this work both as target for generating NPs using PLAL and as electrode for electrocatalytic activity testing.

3.2. Laser-generated MPEA-NPs

Pulse laser ablation was used to synthesize NPs from a homogenized $Al_8Cr_{17}Co_{17}Cu_8Fe_{17}Ni_{33}$ MPEA target in deionized water or in an aqueous solution containing PDADMAC. TEM studies in Fig. 3a and b revealed that the resulting MPEA-NPs synthesized in water (NS-NPs) had a spherical shape and crystalline structure. We used SAXS to estimate the NP concentration and average diameter. This method allows sizing

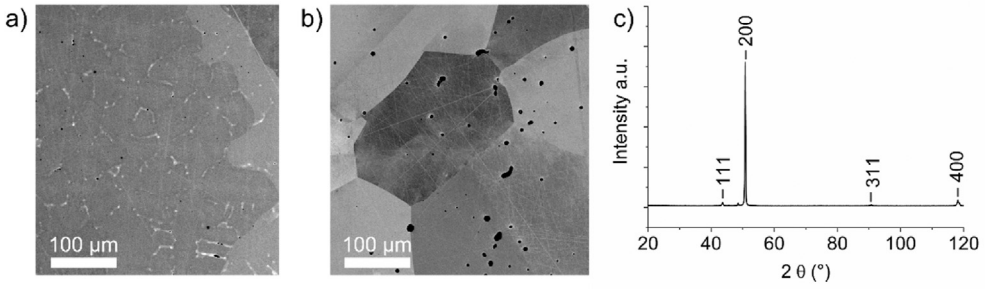

Fig. 1 – SEM images recorded in the back scattered electron (BSE) mode of the $Al_8Cr_{17}Co_{17}Cu_8Fe_{17}Ni_{33}$ a) as-cast and b) after homogenization at 1250 °C for 1 h c) with the corresponding XRD pattern of the sample in b.

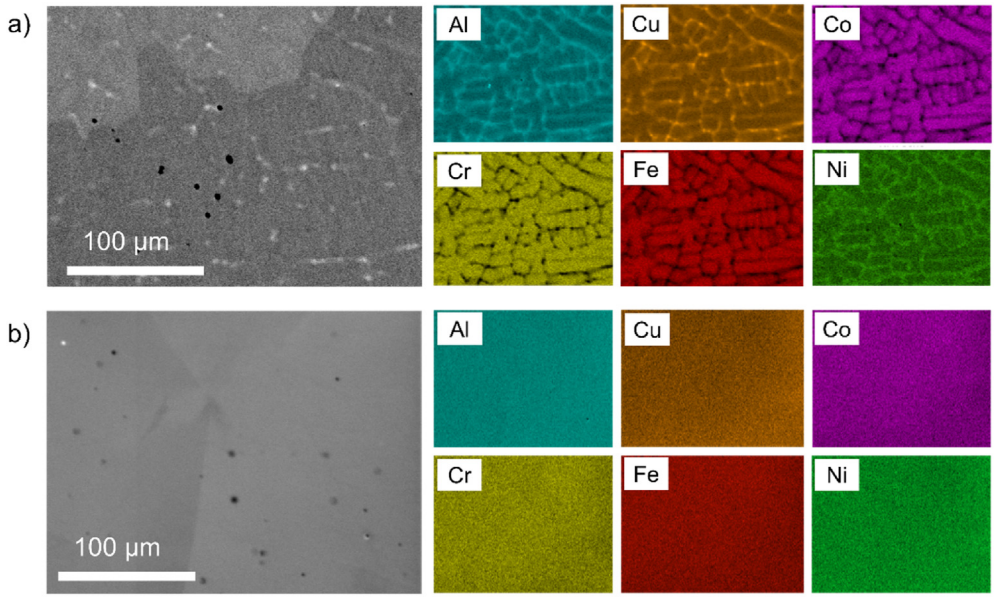

Fig. 2 – EDX maps of the a) as-cast and b) the heat treated $Al_8Cr_{17}Co_{17}Cu_8Fe_{17}Ni_{33}$ MPEA after homogenization at 1250 °C for 1 h.

NPs with diameters ranging from 1 to 100 nm [35,36]. The NP-concentration was found to be $(5.91 \pm 0.18)10^{-4}$ µmol/l or $(9.44 \pm 0.45)10^{-2}$ g/l for NS-NPs, while the average diameter of the resulted particles was (30 ± 4) nm (Fig. 3c). Fig. 3d shows the bright field TEM image and the EDX maps of the NS-NPs confirming the presence of all elements from the MPEA-target in a single NP, but showed that the molar ratio was not preserved, and that phase separation and core-shell morphologies had emerged (Fig. 3a, A), with shells enriched in Al, Cr, Fe and O, and the cores enriched in Ni, Co and Cu. The formation of the core-shell structure and the deviation in the stoichiometry of the resulting NPs can be explained by the differing evaporation enthalpies of Al (293 kJ mol^{-1}), Cr (344 kJ mol^{-1}), Co (382 kJ mol^{-1}), Cu (300 kJ mol^{-1}), Fe (355 kJ mol^{-1}) and Ni (375 kJ mol^{-1}), which can lead to particle disproportionation until solidification during cooling and

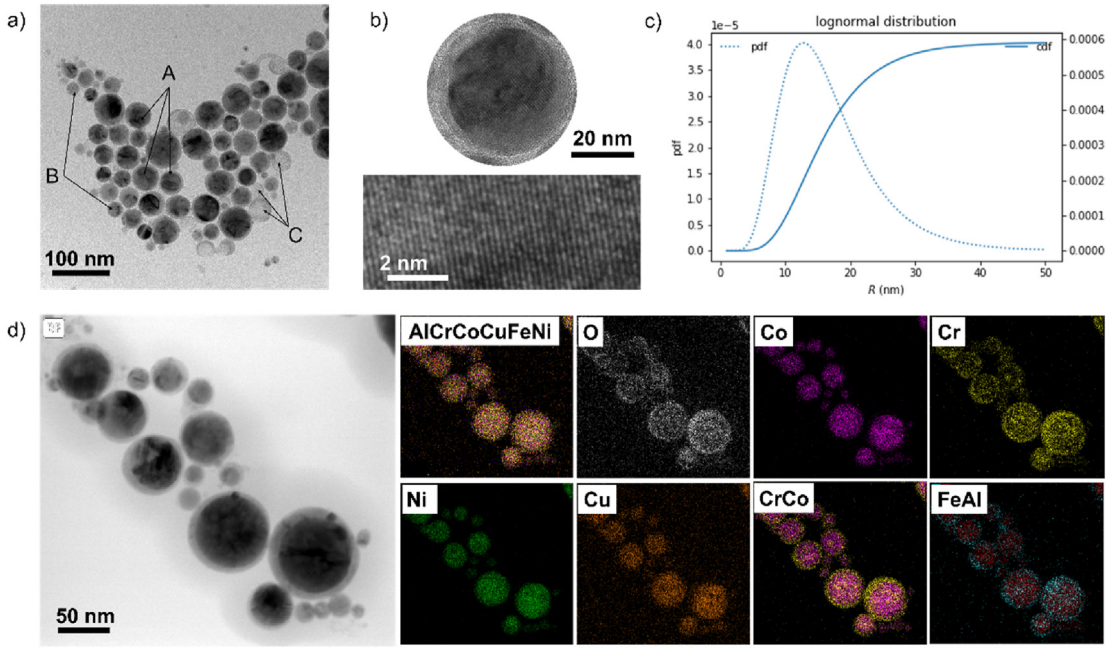

Fig. 3 – a) TEM image of MPEA-NPs synthesized by pulsed laser ablation in pure water (NS-NPs). In b), a single crystalline NP is shown with a magnified section. c) Cumulative diameter distribution (cdf) and partial diameter distribution (pdf) of NS-NPs derived from SAXS employing a lognormal distribution for model calculation d) Bright-field TEM image of NS-NPs and the corresponding EDX maps.

quenching. Jakobi et al. [37,38] have shown that the chemical composition of laser-generated alloy NPs is only preserved for elements with similar enthalpies of vaporization. Moreover, as most of the elements of the MPEA-system tend to oxidize in aqueous solutions, the enrichment of oxide species in the outer shell was expected.

NS-NPs with homogeneous elemental distributions formed less frequently and exhibited diameters >30 nm (Fig. 3a, B), suggesting that the two NP species undergo different formation pathways. Tymoczko et al. [39] observed a similar formation mechanism for FeAu alloy NPs generated by PLAL in acetone and found that the morphology and structure of FeAu NPs was strongly affected by the composition of the alloy target, with the core-shell structure being favored for compositions containing >35 mol% Fe and NP with diameters >10 nm. In further studies, the group demonstrated that it is possible to control the ratio of the core-shell structured NPs and the solid solution NPs using laser pulses with appropriate duration and a target with appropriate structure and composition [40].

In addition to the NS-NPs described above, we also identified a less abundant NP species consisting of a Cr-based core and a Cr oxide shell (Fig. 3a, C). However, the formation mechanism of multi-element NPs by PLALs is not well understood, so it is difficult to determine the driving force behind the formation of this third species. Previous research on laser-assisted synthesis of highly entropic nanomaterials using CoCrFeMnNi has shown that the resulting NPs had a homogeneous distribution of all five elements and a composition that was almost identical to the precursor target [16]. In order to better control the size and structure of NPs synthesized by PLALs, further research is needed to understand the formation mechanism of colloidal MPEA-NPs and identify the key influencing factors such as ablation parameters and target composition.

The synthesis of colloidal NPs often involves the addition of surface ligands that maintain a specific nanostructure and prevent NP-aggregation. The functional role of these ligands has been demonstrated to enhance catalytic activity and control catalyst selectivity through both steric and electronic effects, as referenced in [41–44]. However, surface ligands can also potentially decrease catalytic performance by occupying active surface sites. In our studies, we found that the use of PDADMAC as a stabilizing ligand for MPEA-NPs had no effect on the size or structure of the NPs. Bright-field TEM images and EDX maps revealed that the laser-generated MPEA-NPs in aqueous solution containing PDADMAC (PS-NP) were spherical colloids with predominantly a core-shell structure (Fig. 4a and b). Additionally, it was possible to identify smaller MPEA-NPs with a homogeneous elemental distribution as well as Cr/Cr-oxide core-shell NPs, which is similar to the results obtained with NS-NPs. The concentration of the PS-NPs, as determined using SAXS, was (5.50 ± 0.26) 10^{-4} μmol/l or (1.22 ± 0.11) 10^{-1} g/l (Fig. 4c), a factor of 1.29 higher than that obtained by synthesis in pure water with an average diameter of 39 ± 1 nm.

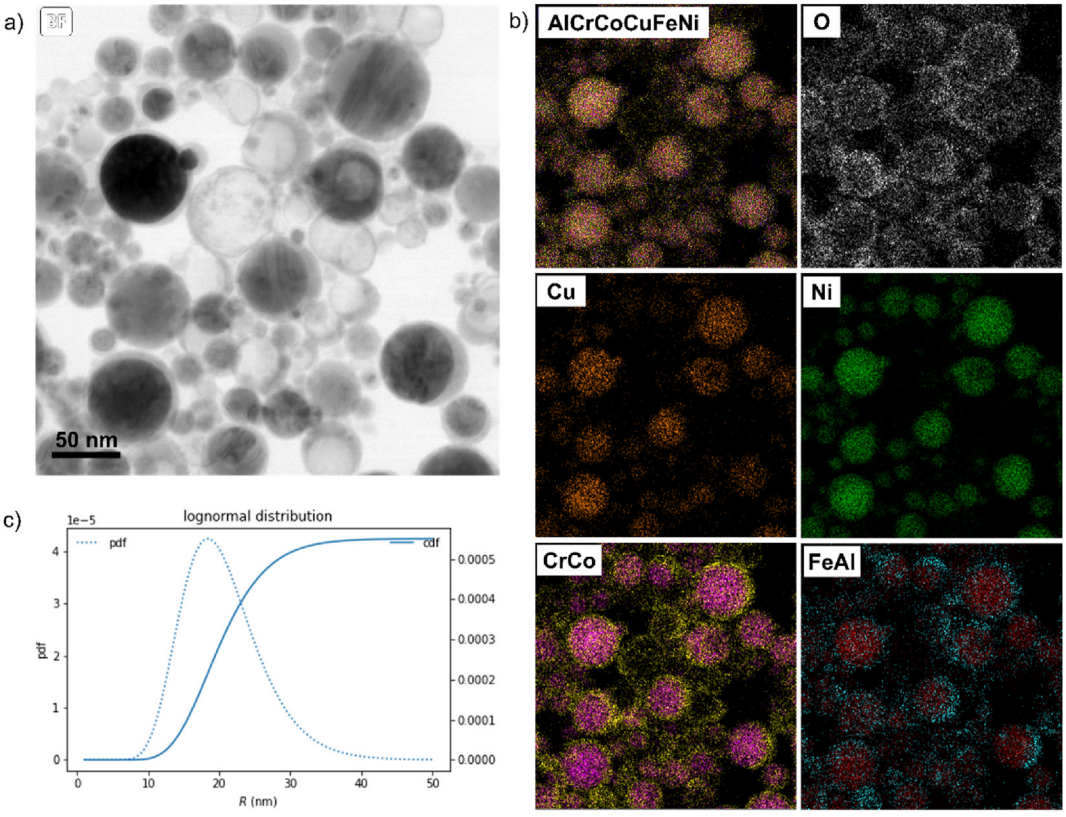

Fig. 4 – a) Bright-field TEM image of MPEA-NPs generated by PLAL in aqueous solution of PDADMAC (PS-NP) and b) the corresponding EDX maps. c) Cumulative diameter distribution (cdf) and partial diameter distribution (pdf) of PS-NP derived from SAXS employing a lognormal distribution for model calculation.

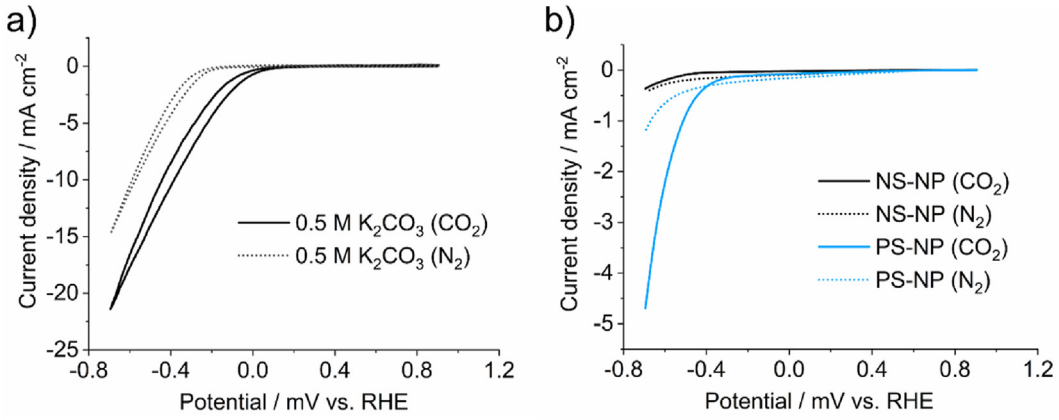

Fig. 5 – a) CV curves for CO_2RR of the $Al_8Cr_{17}Co_{17}Cu_8Fe_{17}Ni_{33}$ MPEA bulk electrode in CO_2- and N_2-saturated 0.5 M K_2CO_3 electrolyte solutions. b) RDE-LSV measurements on the NS-NPs (7.8×10^{-4} mg) and PS-NPs (1.0×10^{-3} mg) deposited on the GC electrode with a surface area of 0.126 cm^2 in CO_2- and N_2-saturated 0.5 M K_2CO_3.

3.3. *Evaluation of the CO_2RR performance*

The electrocatalytic activity was evaluated on MPEA bulk electrodes and NP-electrodes prepared on a GC, RDE using CV or LSV in a CO_2-saturated 0.5 M K_2CO_3 (pH 11.8). As presented in Fig. 5 a, the CV scans on bulk electrodes indicated a high CO_2 activity in K_2CO_3, with an onset potential at −0.08 V vs. RHE. The potential was 200 mV more positive than that onset potential observed in the N_2-saturated electrolyte. The current density at −0.69 V in the CO_2-saturated K_2CO_3 electrolyte was 1.4 times higher (−21.50 mA cm^{-2}) than that observed in N_2-saturated K_2SO_4 (−15.00 mA cm^{-2}).

The LSV curves in Fig. 5b show, that the total current density of the PS-NP outperformed the NS-NP from −0.21 to −0.69 V vs. RHE, reaching a current density as high as −4.69 mA cm^{-2} at −0.69 V in a CO_2-saturated electrolyte solution. The shift in the onset potential of the PS-NP to lower values suggests that PDADMAC-stabilized MPEA-NPs have superior electrocatalytic performance. The surface ligands used obviously promote the catalytic activity of MPEA-NPs. As the stabilization of the NPs with PDADMAC showed no effect on the size and the size distribution of the NPs, we suggest a steric or electronic influence as the reason for the better electrocatalytic performance of the PS-NPs. Recently, Pankhurst et al. [44] demonstrated that surface modification of Ag nanocrystals with imidazolium ligands can significantly improve their electrocatalytic CO_2 activity, which is correlated with the hydrocarbon tail length and the nature of the anchoring group of the ligands. While the cationic imidazolium groups were assumed to promote the accumulation of CO_2 on the catalyst surface, the length of the ligand tail group was found to be key in tuning the hydrophobicity of the surface, thereby further improving the selectivity of the catalyst by suppressing the HER.

The cationic form of PDADMAC may also interact with CO_2 and thus contribute to the improvement in catalyst performance. However, further characterization is needed to fully understand the influence PDADMAC stabilization on catalytic processes.

4. Summary and conclusions

In summary, we synthesized noble metal-free multi-principal element alloy nanoparticles (MPEA-NPs) by pulsed laser ablation in liquids (PLALs) for the electrochemical reduction of CO_2. X-Ray diffraction (XRD) and energy dispersive X-ray (EDX) analysis of the $Al_8Cr_{17}Co_{17}Cu_8Fe_{17}Ni_{33}$ MPEA revealed a single-phase face-centered cubic (fcc)-structure with a homogeneous distribution of elements. However, the molar ratio was not always preserved in the NPs. Transmission electron microscopy (TEM) combined with EDX mapping confirmed the presence of phase separation and the formation of core-shell structure. In addition, small angle X-Ray scattering (SAXS) analysis revealed the particle diameter distribution and the particles number concentration. Electrochemical analysis confirmed a unique activity towards the CO_2 reduction of the poly-(diallyldimethylammonium chloride) (PDADMAC)-stabilized MPEA-NPs. $Al_8Cr_{17}Co_{17}Cu_8Fe_{17}Ni_{33}$ MPEA-NPs have been identified as a highly efficient catalytic system that is able to replace conventional, expensive noble metal electrocatalysts for CO_2 reduction.

Availability of data and material

The datasets used and/or analysed during the current study are available from the corresponding author on reasonable request.

Funding

We would like to thank the ERASMUS + program for supporting the research of Helena Pérez Blanes.

Declaration of competing interest

The authors declare that they have no known competing financial interests or personal relationships that could have appeared to influence the work reported in this paper.

Acknowledgement

The authors thank M. Ebisch and K. Brademann-Jock for the preparation of SAXS measurements.

REFERENCES

[1] Yu LL, Zeng KZ, Li CH, Lin XR, Liu HW, Shi WH, et al. Carbon Energy 2022;4:731–61.
[2] Xin Y, Li SH, Qian YY, Zhu WK, Yuan HB, Jiang PY, et al. ACS Catal 2020;10:11280–306.
[3] Löffler T, Meyer H, Savan A, Wilde P, Garzón Manjón A, Chen Y-T, et al. Adanced Energy Materials 2018;8:1802269.
[4] Xie P, Yao Y, Huang Z, Liu Z, Zhang J, Li T, et al. Nat Commun 2019;10:4011.
[5] Nellaiappan S, Katiyar NK, Kumar R, Parui A, Malviya KD, Pradeep KG, et al. ACS Catal 2020;10:3658–63.
[6] Koenen S, Streubel R, Jakobi J, Schwabe K, Krauss JK, Barcikowski S. J Electrochem Soc 2015;162:D174–9.
[7] Jendrzej S, Gökce B, Epple M, Barcikowski S. ChemPhysChem 2017;18:1012–9.
[8] Crivellaro S, Guadagnini A, Arboleda DM, Schinca D, Amendola V. Rev Sci Instrum 2019;90:033902.
[9] Wagener P, Jakobi J, Rehbock C, Chakravadhanula VS, Thede C, Wiedwald U, et al. Sci Rep 2016;6:23352.
[10] Dittrich S, Kohsakowski S, Wittek B, Hengst C, Gokce B, Barcikowski S, et al. Nanomaterials 2020;10:1582.
[11] Amendola V, Scaramuzza S, Carraro F, Cattaruzza E. J Colloid Interface Sci 2017;489:18–27.
[12] Kazakevich PV, Voronov VV, Simakin AV, Shafeev GA. Quant Electron 2004;34:951–6.
[13] Malviya KD, Chattopadhyay K. J Phys Chem C 2014;118:13228–37.
[14] Nadarajah R, Tahir S, Landers J, Koch D, Semisalova AS, Wiemeler J, et al. Nanomaterials 2020;10:2362.
[15] Mahfouz R, Aires FJCS, Brenier A, Ehret E, Roumie M, Nsouli B, et al. J Nanoparticle Res 2010;12:3123–36.
[16] Waag F, Li Y, Ziefuss AR, Bertin E, Kamp M, Duppel V, et al. RSC Adv 2019;9:18547–58.
[17] Song Y, Junqueira JRC, Sikdar N, Ohl D, Dieckhofer S, Quast T, et al. Angew Chem, Int Ed Engl 2021;60:9135–41.
[18] Zhuang TT, Pang YJ, Liang ZQ, Wang ZY, Li Y, Tan CS, et al. Nature Catalysis 2018;1:946–51.
[19] Li J, Che F, Pang Y, Zou C, Howe JY, Burdyny T, et al. Nat Commun 2018;9:4614.
[20] Wilde P, O'Mara PB, Junqueira JRC, Tarnev T, Benedetti TM, Andronescu C, et al. Chem Sci 2021;12:4028–33.
[21] Morales-Guio CG, Cave ER, Nitopi SA, Feaster JT, Wang L, Kuhl KP, et al. Nature Catalysis 2018;1:764–71.
[22] Zhang H, Chang X, Chen JG, Goddard 3rd WA, Xu B, Cheng MJ, et al. Nat Commun 2019;10:3340.
[23] Castilla-Amoros L, Stoian D, Pankhurst JR, Varandili SB, Buonsanti R. J Am Chem Soc 2020;142:19283–90.
[24] Ren W, Tan X, Qu J, Li S, Li J, Liu X, et al. Nat Commun 2021;12:1449.
[25] Nitopi S, Bertheussen E, Scott SB, Liu X, Engstfeld AK, Horch S, et al. Chem Rev 2019;119:7610–72.
[26] Norskov JK, Bligaard T, Rossmeisl J, Christensen CH. Nat Chem 2009;1:37–46.
[27] Wang CY, Li LL, Yu XF, Lu ZM, Zhang XH, Wang XX, et al. ACS Sustainable Chem Eng 2020;8:8256–66.
[28] Pedersen JK, Batchelor TAA, Bagger A, Rossmeisl J. ACS Catal 2020;10:2169–76.
[29] Orthaber D, Bergmann A, Glatter O. J Appl Crystallogr 2000;33:218–25.
[30] Bressler I, Kohlbrecher J, Thunemann AF. J Appl Crystallogr 2015;48:1587–98.
[31] Yeh JW, Chen SK, Lin SJ, Gan JY, Chin TS, Shun TT, et al. Adv Eng Mater 2004;6:299–303.
[32] Zhou ZM, Gao J, Li F, Wang YP, Kolbe M. J Mater Sci 2011;46:7039–45.
[33] Cao CDD, Sun ZB, Bai XJJ, Duan LBB, Zheng JBB, Wang F. J Mater Sci 2011;46:6203–12.
[34] Fantin A, Lepore GO, Manzoni AM, Kasatikov S, Scherb T, Huthwelker T, et al. Acta Mater 2020;193:329–37.
[35] Pauw BR, Kastner C, Thunemann AF. J Appl Crystallogr 2017;50:1280–8.
[36] Li T, Senesi AJ, Lee B. Chem Rev 2016;116:11128–80.
[37] Jakobi J, Petersen S, Menendez-Manjon A, Wagener P, Barcikowski S. Langmuir 2010;26:6892–7.
[38] Jakobi J, Menendez-Manjon A, Chakravadhanula VS, Kienle L, Wagener P, Barcikowski S. Nanotechnology 2011;22:145601.
[39] Tymoczko A, Kamp M, Prymak O, Rehbock C, Jakobi J, Schürmann U, et al. Nanoscale 2018;10:16434–7.
[40] Tymoczko A, Kamp M, Rehbock C, Kienle L, Cattaruzza E, Barcikowski S, et al. Nanoscale Horizons 2019;4:1326–32.
[41] Schoenbaum CA, Schwartz DK, Medlin JW. Acc Chem Res 2014;47:1438–45.
[42] Liu P, Qin R, Fu G, Zheng N. J Am Chem Soc 2017;139:2122–31.
[43] Zhu Q, Murphy CJ, Baker LR. J Am Chem Soc 2022;144:2829–40.
[44] Pankhurst JR, Guntern YT, Mensi M, Buonsanti R. Chem Sci 2019;10:10356–65.